Materials Research Proceedings 57 (2025) 319-326 https://doi.org/10.21741/9781644903735-37

Numerical modeling of high-speed laser cutting of copper current collectors

Samuele Piandoro[1,a *], Caterina Angeloni[1,b], Alessandro Fortunato[1,c], Erica Liverani[1,d], Alessandro Ascari[1,e]

[1]Department of Industrial Engineering (DIN), Alma Mater Studiorum University of Bologna, Viale Risorgimento 2, 40136 Bologna, Italy

[a]samuele.piandoro2@unibo.it, [b]caterina.angeloni2@unibo.it, [c]alessandro.fortunato@unibo.it, [d]erica.liverani2@unibo.it, [e]a.ascari@unibo.it

Keywords: Laser Cutting, Copper, Multi-Physics Simulation, Process Optimization

Abstract. The increasing demand for lithium-ion batteries requires precise, efficient cutting of copper current collectors. Laser cutting offers advantages over mechanical methods in terms of speed, precision, and flexibility. This study uses validated multi-physics simulations to model the interaction between a single-mode continuous laser and 8 μm copper foils, analyzing how power, speed (up to 25 m/s), and foil thickness affect cut quality. Four outcomes were identified: no cut, dross, spatter, and clean cuts. Process maps for 8 μm and 16 μm foils were derived, offering insights for optimizing battery manufacturing.

Introduction

To meet the increasing demands for productivity and quality in lithium-ion battery production and assembly, optimizing the manufacturing process is essential. Among the various steps, trimming the current collectors (thin conductive metal foils) is one of the most delicate. Laser beam cutting is a state-of-the-art technique due to its ability to provide higher processing speed and quality compared to traditional methods [1], [2]. However, as a thermal process, it is inherently associated with defects in the edge profile, such as spatter, dross, and uneven kerf, which can negatively impact battery performance.

Dross formation is particularly undesirable, as detached particles can mix with the electrode slurry, creating preferential pathways for metallic deposition. Over multiple charge/discharge cycles, this may lead to dendrite growth, which can pierce the separator and cause short circuits, ultimately resulting in premature battery failure or even explosions.[3], [4].

Spatter occurs when the local momentum of the molten material exceeds a threshold, represented by the dimensionless Weber number (We >> 2) [5], [6]. The primary force driving this process is the recoil pressure caused by the almost instant vaporization of the material.

Although ultra-short, pulsed beams (e.g., picosecond and femtosecond lasers) have been extensively studied with good results [7], [8], their high cost and low productivity make them unattractive from an industrial perspective. In a previous study [9], the authors compared the cutting quality between a continuous source and a commercial nanosecond pulsed source, showing that the single-mode continuous source yields higher quality.

Numerous models [10], [11], [12] have been developed to simulate the laser cutting process of thick sheets; however, while they are valuable for understanding certain melt flow dynamics, they fall short in addressing the unique challenges of processing thin foils such as current collectors. Only a few have been applied to current collectors and micrometer-thick electrodes. In this context, Lee et al. [13] is, to the author's knowledge, the only existing application of a 3D consistent numerical model [14] for the laser cutting of current collectors and electrodes. However, his study was limited to relatively low power and speed, reaching a maximum of 300 W and 5 m/s.

In this research, we developed a CFD framework for simulations of laser-material interactions using the well-known volume of fluid (VOF) method to predict defects occurring during the laser cutting of pure copper current collectors. The model was tuned and validated against experimental results and subsequently used to analyze and compare outcomes at different process parameters and foil thicknesses. As a result, a power-speed graph was generated for 8 µm and 16 µm foil thicknesses.

Materials and methods

Experimental procedure

The laser system employed was a continuous wave nLight 1200 W single-mode, equipped with a 14 µm optical fiber and scanning head with a 340 mm f-theta lens (the actual setup is shown in Fig. 1A). The spot size was measured as 65 µm with an $M^2 \leq 1.1$. Current collectors of pure copper 8 µm thick were cut from rolls and kept in a clamping system to maintain the foils stretched out in the focal plane. Linear and parallel cuts 20 mm long were performed with 5 mm distances between adjacent cuts (Fig. 1B). The parameters measured for defect analysis and quality assessment are shown in Fig.1C, four parameters were evaluated: i) dross thickness (front m_1 and back m_2), ii) remelted area, iii) spatter max distance, and iv) kerf width.

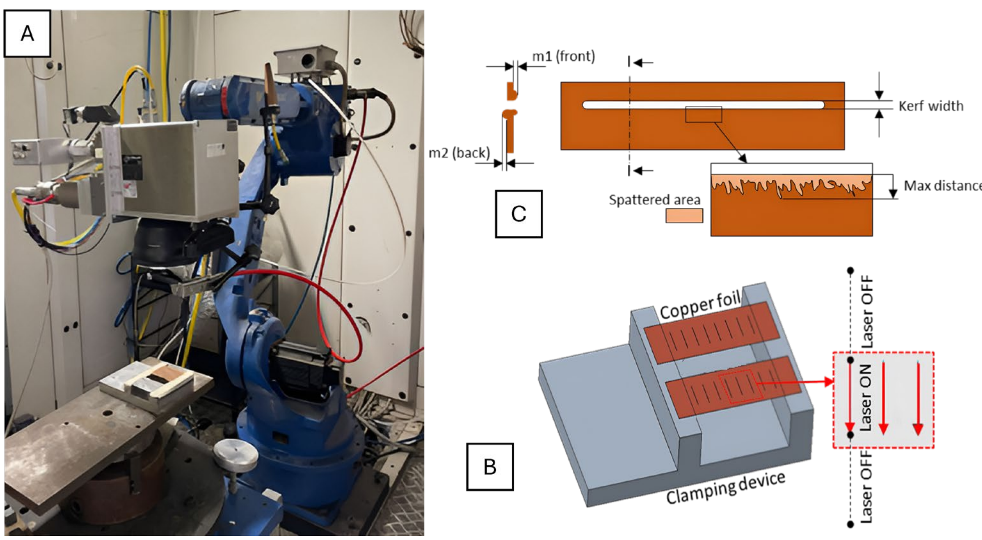

Figure 1: Experimental setup (A), cutting geometry (B), and parameters evaluated (C).

The operative range investigated was selected based on the previous study [1] and constrained by the limitations of the experimental setup. The power and velocity ranges were set to [200–1000] W and [2–25] m/s, respectively. Five representative cases were then selected for the calibration (three cases) and validation (two cases) of the numerical model. Each case exhibits distinct outcomes in terms of cut quality and defect formation: case A: bubble-shaped recast, case B: good cut, case C: spatter, case D: wide kerf with burn, and case E: no cut. These cases correspond to the extreme values of the operative window — i.e., minimum and maximum values of power and velocity — except for the 'no cut' condition, where the first velocity value leading to a failed cut was identified and used. This selection was intended to ensure the model's robustness across a wide range of operative conditions. The corresponding process parameters and experimental outcomes for each case are summarized in Table 1, where the irradiance (I) and fluence (F) were calculated as follows:

Materials Research Proceedings 57 (2025) 319-326 https://doi.org/10.21741/9781644903735-37

$$I = \frac{P}{A_{spot}} \left[\frac{W}{cm^2}\right] \qquad F = I \cdot \tau = I \cdot \frac{d_{spot}}{v} \left[\frac{J}{cm^2}\right] \tag{1}$$

Where τ is the interaction time calculated from the spot diameter and the laser velocity.

Table 1: Process parameters employed for laser cutting tests.

	P [W]	Laser speed [m/s]	I [MW/cm²]	F [J/cm²]	Model	Defect
A	200	2	6.0	195.9	Tuning	Bubble Recast
B	600	10	18.1	117.5	Tuning	Good Cut
C	1000	25	30.1	78.4	Tuning	Spatter
D	1000	2	30.1	979.4	Validation	Burn
E	200	5	6.0	78.4	Validation	No Cut

Optical microscopy (OM, Nikon Optiphot-100) and SEM-FEG microscopy (SEM, Tescan Mira3 with a Schottky emitter) were used to evaluate the cutting quality. OM was initially used to provide a preliminary assessment of cut quality. Hence, high-quality images for spatter quantification and kerf measurements were carried out with SEM on the same surfaces.

To quantify the remelted area, the experimental images were processed with Trainable Weka Segmentation, a Fiji plugin [2]. The Fast Random Forest machine learning algorithm was applied as the classifier to be trained on one SEM image given as input. Three classes were therefore selected for input labelling: kerf, surface and remelted area. Once the model was confirmed to make accurate predictions, the area with an 80-100% probability of belonging to the spatter class was measured.

The spatter maximum distance was defined as the greatest distance measured from the cut edge to the furthest melted metal finger lying on the copper foil. Data was collected through SEM image analysis, with three SEM images acquired from the front and three from the back of the cut. For each image analyzed, three measurements were taken, and the maximum value, along with the standard deviation of these measurements, was calculated.

The same images were used for average kerf width comparisons, both on the top and back of the surface, and the mean value was calculated considering five measurements for each picture.

After non-destructive cut analysis, the current collectors were sectioned and embedded in resins for dross height measurements (m_1 and m_2 in Fig. 1C). By polishing the samples, it was possible to evaluate the mean dross thickness in the middle section of the cut (20 measurements were taken for each cut condition).

Numerical Model

The laser cutting process was simulated using the commercial CFD software FLOW-3D (v12.0 Update 3) with the laser module FLOW-3D WELD (release 7 Update 3). FLOW-3D employs the finite volume method and implements an advanced Volume of Fluid (VoF) algorithm to track phase boundaries. This model defines a scalar function F_i representing the fraction of phase i within a computational cell. The sum of all phase fractions in each cell must equal one; therefore, by considering only the metal and the surrounding air as distinct phases, we obtain:

$$\begin{cases} F = 0 & metal \\ 0 < F < 1 & interface \\ F = 1 & air \end{cases} \tag{2}$$

The conservation of F is governed by the following equation:

$$\frac{\partial F}{\partial t} + u\frac{\partial F}{\partial x} + v\frac{\partial F}{\partial y} + w\frac{\partial F}{\partial z} = 0 \quad (3)$$

Where u, v, and w are the velocity components of the flow field.

The simulation incorporates the main physical phenomena governing laser cutting, including viscous laminar flow, energy conservation with phase change, volumetric thermal expansion, temperature-dependent surface tension with Marangoni forces, multiple laser reflections with temperature-dependent absorption, and evaporation-driven recoil pressure.

Recoil pressure is the key driver of material ejection in laser cutting, it arises from the rapid vaporization of the molten material, generating a force that pushes the liquid metal away from the laser focus. This force modeled empirically based on the Clausius-Clapeyron relation and follows the equation:

$$P_{recoil} = C_1 exp C_2 \left(1 - \frac{T_v}{T}\right) \quad (4)$$

C_1 and C_2 are parameters that must be tuned through experimental results, while T_v refers to the saturated curve provided by the Clausius-Clapeyron equation. The influence of the plasma plume, which affects laser absorption and energy distribution, is indirectly incorporated through a temperature-dependent absorption coefficient, following approaches previously validated in the literature [11]. The laser beam is modeled as multiple rays propagating along the z-axis, interacting with the material based on the temperature-dependent absorption coefficient. Absorbed energy induces heating, melting, and evaporation, whereas reflected rays, guided by the local surface normal, redistribute energy through multiple reflections, shaping the keyhole and influencing cutting quality. Material properties for pure copper, including thermal conductivity, density, specific heat, surface tension, and viscosity, were sourced from the literature [12]. These properties were integrated as temperature-dependent functions to ensure an accurate representation of material behavior under laser irradiation. To keep the text concise, only the main models are mentioned without detailing all equations and numerical implementation. However, the implementation follows similar studies where FLOW-3D was utilized for laser welding simulations; readers can refer to [11] and [13].

By considering the process symmetrical to the laser direction (x-axis), only half of the domain can be discretized, which reduces the total number of cells and computational cost. A staggered Cartesian grid composed of two nested regions was created (Figure 2): a main region measuring 0.1 mm x 0.15 mm x 0.1 mm with a 1.5 µm cell size, and a thermal diffusion region that is 0.1 mm larger in the x and y dimensions with a cell size five times larger. The main region captures the laser-current interaction and, therefore, requires a finer mesh, while the thermal diffusion region only accounts for heat transfer. A constant atmospheric pressure (101325 Pa) was applied to both the top and bottom surfaces and fixed walls on the remaining sides, but the symmetric plane.

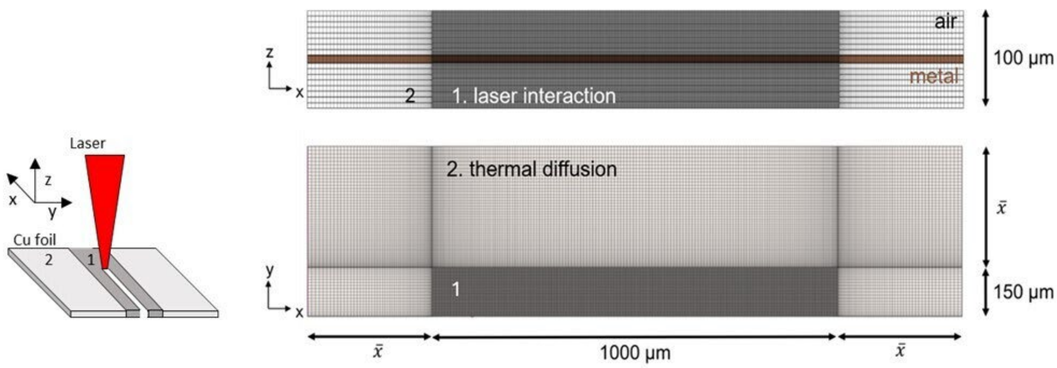

Figure 2: Computational Domain

Cut conditions

The developed framework simulated laser cutting of pure copper current collectors across all the entire range of process parameters shown as black dots in Fig. 3. The tuning conditions, detailed in Table 1, are represented by red dots, while blue squares indicate the validation cases.

The same process parameters were selected to evaluate the effect of cutting as the current collector thickness increases from 8 to 16 µm.

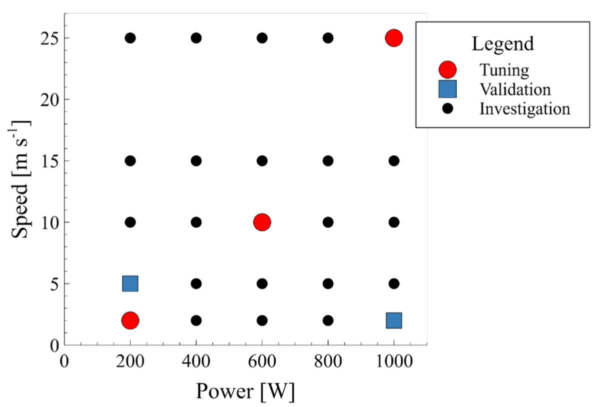

Figure 3: Simulated cut conditions

Results and discussion

The experimental cuts exhibit distinct defect patterns, as shown in Figure 4. SEM images reveal bubble-shaped recast and an uneven kerf width in cut A, resulting from low speed and power, which promote melting over vaporization. In contrast, cut C shows spatter formation, as high speed and power enhance the ejection of metal droplets. Cut B demonstrates good quality, with dross limited to the back surface, as seen in the optical microscope image. Among the validation conditions, cut E fails to reach the melting and vaporization temperatures and is therefore not included in Figure 4 below, Cut D represents an intermediate case, displaying dross on both surfaces, a nearly constant kerf width, and no spatter.

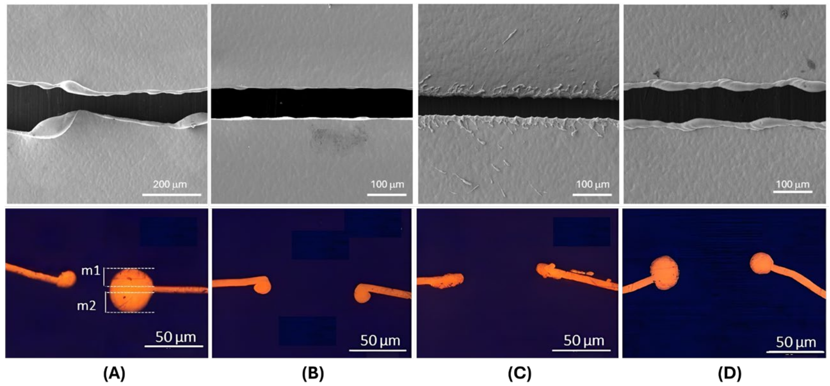

Figure 4: SEM images of front surface (first row) and optical images of edge profile (second row) for tuning and validation cuts

Model tuning and validation

Given the wide range of power and speed investigated—and consequently, the significant variation in fluence and irradiance—a single set of parameters C_1 and C_2 for the recoil pressure (equation 4) did not yield accurate results across the entire process window. Therefore, C1 was tuned with a power trend against the fluence and C2 with a linear trend against the irradiance. The following equations were found:

$$C_1 = 14.4E^7 \cdot F^{-1.18} \quad (5)$$
$$C_2 = 0.358 \cdot I + 0.068 \quad (6)$$

The quantitative evaluation of the data matching between the model and experiments can be seen in Figure 5, with the mean value and the standard deviation obtained through the 160 total measurements as specified in the Materials and Methods section.

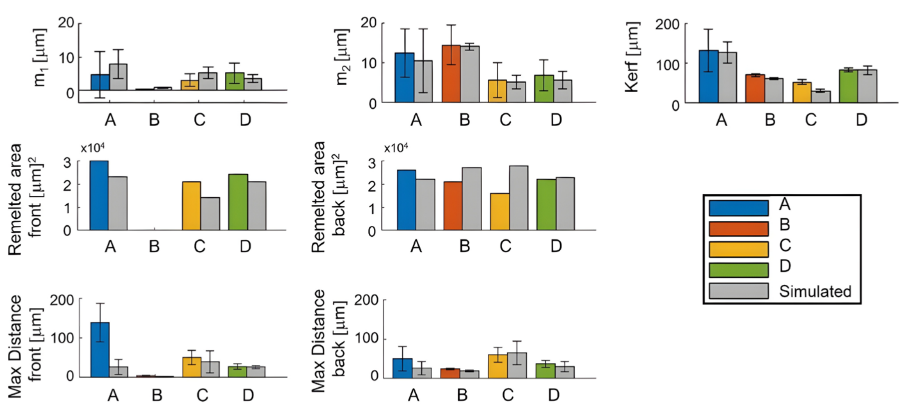

Figure 5: Comparison between simulated and experimental cut by kerf, dross measurements, and spatter area and distance

Overall, the model demonstrates good agreement with the experimental results across all metrics and test cases, as shown in Fig. 5. The simulated values generally follow the same trend as the experimental data, with differences that fall within the standard deviation of the measurements. The only noticeable discrepancy concerns the "Max Distance front" in case A, where the model underestimates the experimentally observed values. This deviation is attributed to the limited mesh resolution and computational domain size, which were optimized to capture the phenomena occurring near the laser–material interaction zone, while high-velocity spatters may exit the domain before being tracked.

Cutting quality prediction

Once the robustness of the model in accurately predicting the laser-current collector interaction was established, the influence of power, speed, and foil thickness on defect formation was investigated. The cutting quality was divided into five different conditions: No cut, Recast, Dross, Good, and Spatter. Figure 6 shows the results for both foil thicknesses in the total parameters window.

For the 8 μm case, the figure shows both the SEM and simulation results, while for the 16 μm only simulations were performed as no foil with this value of thickness was available.

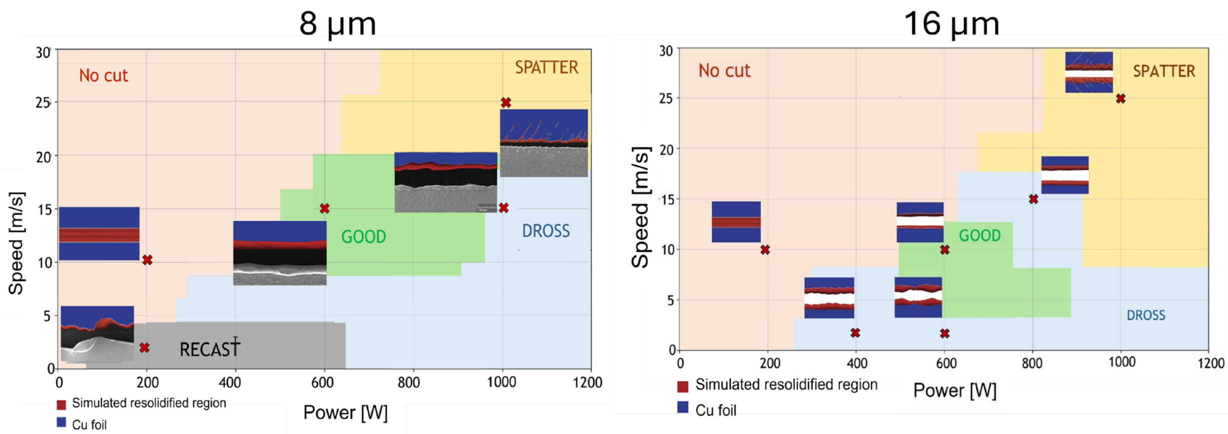

Figure 6: Cut quality prediction for 8 and 16 μm

The analysis of the kerf width, dross formation, and spatter behavior across different process parameters reveals clear trends in cut quality. At lower power and speed levels, the formation of recast material is prevalent due to the instability of the molten region, leading to high kerf variability and significant standard deviations in m_1 and m_2. As power increases, the transition from recast to dross-dominated regions occurs, with dross height exceeding critical thresholds relative to foil thickness. At higher speeds, particularly above 19 m/s, spatter formation becomes evident, mainly at the back of the cut, as the melt ejection becomes irregular. Increasing power beyond 1000 W further exacerbates droplet ejection at the front, confirming a shift in defect behavior.

The definition of the good cut region highlights the importance of both kerf stability and minimal dross accumulation. In this optimal range, front dross is nearly absent, kerf width remains uniform, and molten material is confined close to the cutting edge. However, a further increase in power, even within this stable region, can negatively impact edge quality, leading to the onset of dross formation.

It is important to highlight that the model was calibrated using a specific laser source and copper foil, and its predictive capabilities are currently limited to the tested operating conditions. The empirical coefficients adopted in the CFD formulation were fitted using experimental data representative of distinct cutting regimes; however, these values may not generalize to significantly different materials or beam configurations. A broader generalization would require additional parameters that explicitly account for material and source variability.

The effect of foil thickness was also examined by doubling the thickness from 8 μm to 16 μm. The results indicate a shift in the process window, with a general increase in dross formation and a reduction in the range of process parameters that yield a good cut. The higher thermal mass of the thicker foil affects heat dissipation, requiring an adjustment of power and speed combinations to maintain an optimal cut. While good cut conditions are still achievable, the increased tendency for spatter and dross at higher powers and speeds suggests a narrower operating range for achieving high-quality cuts in thicker foils.

Conclusion

In this study, the developed CFD model successfully predicted the behavior of CW laser cutting of thin copper foils used as current collectors in lithium-ion battery electrodes. After tuning and validating the model with experimental results, it was possible to investigate the influence of laser power, speed, and foil thickness on cut quality, including kerf dimensions, dross formation, and spatter behavior. The threshold laser parameters for achieving high-quality cuts were identified, as well as the conditions leading to defect formation. Experimental results revealed the presence of spatter, dross, and recast material, which the model accurately captured, confirming its reliability in predicting defect-prone regions. By analyzing the interplay of process parameters, this study identified key physical mechanisms responsible for defect formation and provided predictive equations for determining process windows that minimize unwanted effects. The findings offer a valuable reference for optimizing laser cutting conditions, ensuring quality even when input parameters such as material properties, spot size, or thickness vary. This approach reduces the need for extensive experimental testing, offering a more efficient path to process optimization.

References

[1] C. Angeloni, E. Liverani, A. Ascari, A. Fortunato, J. Mater. Process. Technol. 324 (2024) 118266. https://doi.org/10.1016/j.jmatprotec.2023.118266

[2] J. Schindelin, I. Arganda-Carreras, E. Frise, V. Kaynig, M. Longair, T. Pietzsch, S. Preibisch, C. Rueden, S. Saalfeld, B. Schmid, J.-Y. Tinevez, D.J. White, V. Hartenstein, K. Eliceiri, P. Tomancak, A. Cardona, (2012).

[3] M. Luetke, V. Franke, A. Techel, T. Himmer, U. Klotzbach, A. Wetzig, E. Beyer, Phys. Procedia 12 (2011) 286-291. https://doi.org/10.1016/j.phpro.2011.03.135

[4] W. Schulz, V. Kostrykin, M. Nießen, J. Michel, D. Petring, E.W. Kreutz, R. Poprawe, J. Phys. Appl. Phys. 32 (1999) 1219-1228. https://doi.org/10.1088/0022-3727/32/11/307

[5] W. Pfleging, Nanophotonics 7 (2018) 549-573. https://doi.org/10.1515/nanoph-2017-0044

[6] M.J. Assael, A.E. Kalyva, K.D. Antoniadis, R. Michael Banish, I. Egry, J. Wu, E. Kaschnitz, W.A. Wakeham, J. Phys. Chem. Ref. Data 39 (2010) 033105. https://doi.org/10.1063/1.3467496

[7] X. Zhu, D.M. Villeneuve, A.Y. Naumov, S. Nikumb, P.B. Corkum, Appl. Surf. Sci. 152 (1999) 138-148. https://doi.org/10.1016/S0169-4332(99)00331-1

[8] C. Hartmann, J. Laser MicroNanoengineering 8 (2013) 266-270. https://doi.org/10.2961/jlmn.2013.03.0013

[9] J. Grabow, J. Klink, R. Benger, I. Hauer, H.-P. Beck, Batteries 9 (2022) 9. https://doi.org/10.3390/batteries9010009

[10] Y. Yuan, H. Wang, X. Han, Y. Pan, Y. Sun, X. Kong, L. Lu, M. Ouyang, Appl. Energy 361 (2024) 122968. https://doi.org/10.1016/j.apenergy.2024.122968

[11] G. Chianese, S. Jabar, P. Franciosa, D. Ceglarek, S. Patalano, Procedia CIRP 111 (2022) 484-489. https://doi.org/10.1016/j.procir.2022.08.075

[12] S.P. Lin, R.D. Reitz, Annu. Rev. Fluid Mech. 30 (1998) 85-105. https://doi.org/10.1146/annurev.fluid.30.1.85

[13] W. Huang, H. Wang, T. Rinker, W. Tan, Mater. Des. 195 (2020) 109056. https://doi.org/10.1016/j.matdes.2020.109056